

# End-to-End Inverse Designed Metasurfaces for Snapshot RGB-Achromatic Full-Stokes Polarization Imaging

XINGYU CHAI,<sup>1</sup> JIRONG BAO,<sup>1</sup> HAINING YANG,<sup>1</sup> AND MENGDI SUN<sup>1,\*</sup>

<sup>1</sup>*Department of Electronic and Science and Engineering, Southeast University, Nanjing, Jiangsu, China  
smd@seu.edu.cn*

**Abstract:** Snapshot full-Stokes polarimetry across multiple wavelengths remains challenging because conventional architectures rely on multiplexed measurements and bulky optics. We present an end-to-end framework that reconstructs RGB full-Stokes images from a single monochrome sensor measurement. The system combines a differentiable  $4f$  optical frontend with a U-Net backend for joint optimization. A metasurface modeled by the multilayer perceptron (MLP) is employed to encode the full-Stokes polarization information. We implement the design in two stages: first in a hybrid metasurface-refractive  $4f$  architecture, and then in a pure meta-optic configuration. On a real-world dataset, the hybrid metasurface-refractive system achieves 30.00 dB peak signal-to-noise ratio (PSNR) and 0.8291 structural similarity index measure (SSIM) for monochromatic imaging in the visible range, and 26.71 dB/0.7044 for RGB-achromatic imaging. The pure meta-optic system yields 26.94 dB/0.7184 for the monochromatic case and 24.10 dB/0.6015 for the RGB-achromatic case. These results show that end-to-end optical-digital co-design enables high-performance snapshot full-Stokes polarimetric imaging at a high compression ratio of 12.

## 1. Introduction

Polarization imaging provides information beyond conventional intensity imaging by probing the vector nature of light. In particular, full-Stokes measurements capture both linear and circular polarization components and therefore enable richer characterization of surface roughness [1], depolarization [2], multiple scattering [3–5], and chiral or anisotropic responses [6–9], with applications ranging from scene understanding and remote sensing to imaging in challenging environments [10–12]. However, most full-Stokes imaging systems still rely on spatial or temporal multiplexing using polarizers [13], wave plates [14], or division-of-focal-plane architectures [15]. These strategies typically increase system complexity and often sacrifice light throughput, spatial resolution, or snapshot capability, which limits their use in compact and high-speed imaging platforms [16–18].

Metasurfaces offer a promising route to compact polarization-sensitive optics because sub-wavelength meta-atoms can tailor amplitude, phase, and polarization response within an ultrathin form factor [19, 20]. This capability has motivated a broad range of meta-optic polarization and spectro-polarimetric devices [21–23]. Yet many existing systems prescribe the optical response a priori and treat reconstruction as a separate downstream problem, or they target only part of the polarization state. For snapshot full-Stokes imaging, especially when spectral information is also encoded, such separately designed systems can lead to a poorly conditioned inverse problem that is sensitive to noise, model mismatch, and spectral-polarimetric crosstalk [17].

In parallel, computational imaging has increasingly shifted from post hoc reconstruction to optical-digital co-design, in which the optical frontend and the reconstruction backend are optimized jointly for a target inference task [24]. Recent work has shown that meta-optics can serve not merely as miniature replacements for conventional optics, but as task-specific physical encoders trained together with the reconstruction algorithm [25–29]. This perspective is particularly compelling for full-Stokes imaging, where the sensor measurement is intrinsically

compressive and the reconstruction quality depends as much on the optical encoding as on the computational backend.

Here we present an end-to-end meta-optic framework for snapshot RGB-achromatic full-Stokes polarization imaging. Our system combines a differentiable  $4f$  frontend with a trainable metasurface at the Fourier-plane and a U-Net reconstruction backend. To minimize the computational cost and make the pipeline compatible with gradient-based optimization, we use a multilayer perceptron (MLP)-based surrogate model to predict the polarization response of the meta-atoms instead of running expensive numerical solvers. We implement the design in two stages: first in a hybrid metasurface-refractive  $4f$  architecture, and then in a pure meta-optic configuration in which the refractive lenses are replaced by metalenses. In the first stage, the metasurface geometry, the focal length, and the neural-network weights are co-optimized. In the second stage, the metalens geometries are additionally optimized with the focal length replaced by free-space distances. On a real-world spectro-polarimetric dataset [30], the hybrid system reaches 30.00 dB PSNR and 0.8291 SSIM in the monochromatic case and 26.71 dB and 0.7044 across three RGB wavelengths; the pure meta-optic system retains strong performance, achieving 26.94 dB and 0.7184 for monochromatic imaging and 24.10 dB and 0.6015 for RGB imaging at a relatively high compression ratio of 12. These results show that end-to-end co-design opens a new avenue for compact, snapshot, high-dimensional polarimetric imaging in both hybrid and pure meta-optic systems.

## 2. Method

Our framework combines a differentiable optical encoder with a neural decoder for snapshot full-Stokes polarization imaging. The optical frontend is based on a  $4f$  system with a trainable polarization-sensitive metasurface placed at the Fourier plane, and the computational backend is a U-Net that reconstructs the full-Stokes image cube from a single sensor measurement. To enable efficient end-to-end optimization, both the Fourier-plane metasurface and the metalenses are modeled through an MLP-based surrogate trained on full-wave electromagnetic simulations. In Section 2.1, we detail the design process of the MLP-based surrogate model for the metasurface and the metalenses, as shown in Fig. 1. In Sections 2.2-2.4, we introduce the inverse design framework for full-Stokes polarization imaging, detailing its optical frontend, computational backend and the end-to-end optimization pipeline, as shown in Fig. 2. Notably, the optimization is performed in two stages, as shown in Table 1. In the first stage, a hybrid metasurface–refractive  $4f$  system is optimized by jointly updating the metasurface geometry, the focal length, and the neural-network weights. In the second stage, the refractive lenses are replaced by two metalenses for further CMOS process compatibility and suitability for massive production, and the meta-optic  $4f$  system is re-optimized by jointly updating the metalens geometries, the metasurface geometry, the free-space distances, and the neural-network weights.

Table 1. The optical differentiable configuration corresponding to two stages.

Stage	Optical configuration
First stage (metasurface-refractive $4f$ system)	metasurface geometry, focal length, neural-network weights
Second stage (meta-optic $4f$ system)	metalens geometries, metasurface geometry, free-space distances, neural-network weights

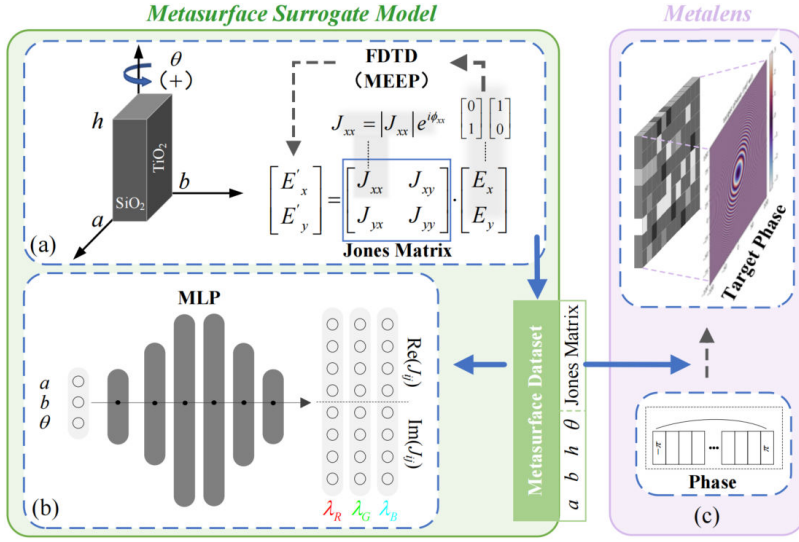


Fig. 1. The design process of the MLP-based surrogate model for the metasurface and the metalenses.

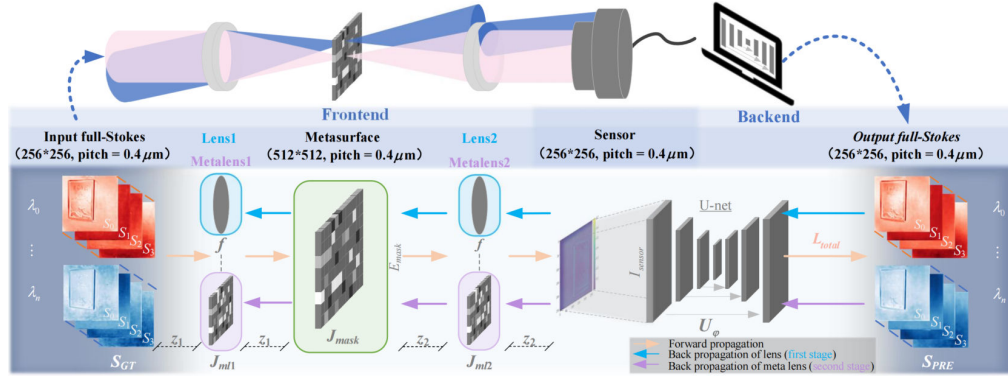


Fig. 2. The architecture of the proposed full-Stokes polarization imaging system

### 2.1. Design of meta-optics

The MLP-based surrogate model characterizes the responses of the subwavelength unitcells (meta-atoms) of the metasurface corresponding in the RGB-achromatic case [31, 32]. As shown in Fig. 1a, each meta-atom consists of a TiO<sub>2</sub> rectangular nanopillar on a SiO<sub>2</sub> substrate. The refractive indices of TiO<sub>2</sub> and SiO<sub>2</sub> are taken as 2.55 and 1.45, respectively [33]. The nanopillar height is fixed at 0.8 μm for ease of fabrication, whereas the in-plane geometrical parameters, namely the length  $a$ , width  $b$ , and rotation angle  $\theta$ , are treated as degrees of freedom. The parameters  $a$  and  $b$  are varied within the range of 0.05–0.4 μm, and  $\theta$  is swept from 0° to 90°. The unit-cell period is fixed at 0.4 μm to suppress higher-order diffraction.

For each meta-atom, the local polarization response is described by a  $2 \times 2$  complex Jones matrix under a complete polarization basis [34]:

$$J(a, b, \theta) = R(-\theta) \begin{bmatrix} e^{i\phi_x(a,b)} & 0 \\ 0 & e^{i\phi_y(a,b)} \end{bmatrix} R(\theta) \quad (1)$$

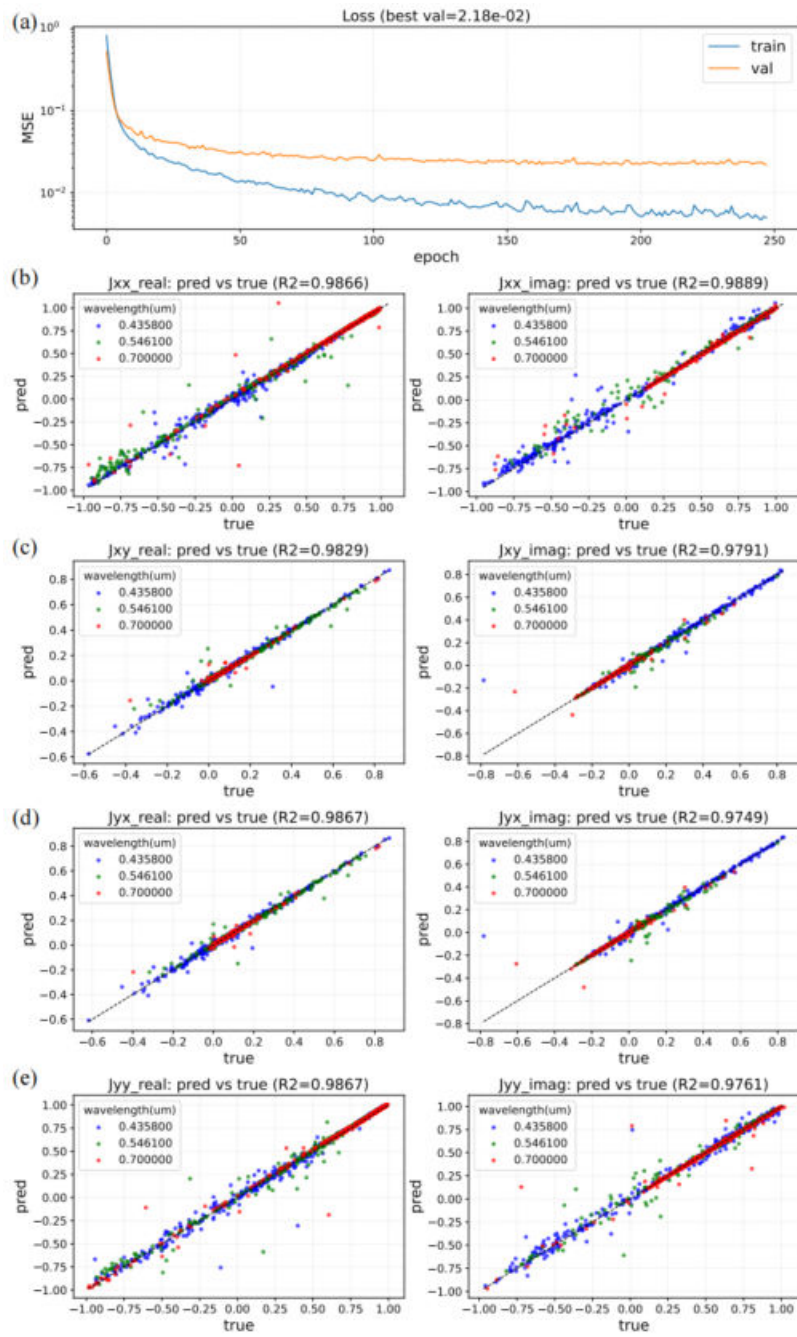


Fig. 3. Performance of the MLP-based surrogate model based on the meta-atoms of the metasurface at RGB-achromatic case. (a) Training and validation loss over training epochs. (b-e) Scatter plots of predicted vs. true values (real and imaginary components of the Jones matrix).

where the matrix elements encode the amplitude and phase response for orthogonal polarization components.  $\phi_x$  and  $\phi_y$  represent the phase shifts introduced along the nanopillar’s principal axes, which are sensitive to  $a$  and  $b$ .

To generate the surrogate-model dataset, we perform full-wave electromagnetic simulations using the finite-difference time-domain (FDTD) solver in MEEP under the locally periodic approximation (LPA) [35, 36]. LPA is widely used in the design of conventional metasurfaces comprised of nanopillars or nanofins, in which non-local coupling between adjacent meta-atoms is negligible [37–40]. Two orthogonal linearly polarized incident fields,  $[1, 0]^T$  and  $[0, 1]^T$ , are used to extract the complex Jones matrices at the RGB-achromatic case. The resulting dataset establishes the mapping between meta-atom geometry and polarization response.

The MLP-based surrogate model is then trained to approximate this mapping, as illustrated in Fig. 1b. The input to the MLP is the set of geometrical parameters  $\{a, b, \theta\}$ , and the output is the real and imaginary parts of the Jones-matrix elements at the target wavelengths. Once trained, the surrogate model replaces repeated full-wave simulations during system-level optimization and enables efficient backpropagation through the optical frontend. The training loss is defined as the mean squared error (MSE) between the predicted and simulated Jones-matrix elements. The network is trained via custom gradient descent with a learning rate of  $10^{-3}$  and an early stop mechanism, using a training/validation/test data split of 8:1:1.

The predictive accuracy of the surrogate model is summarized in Fig. 3. As shown in Fig. 3(a), the training loss decreases below  $10^{-2}$ , while the validation loss remains below  $10^{-1}$  by the end of training. The regression plots in Fig. 3(b-e) further confirm strong agreement between simulated and predicted Jones-matrix elements, with the  $R^2$  values around 0.98 across the real and imaginary parts of  $J_{xx}$ ,  $J_{xy}$ ,  $J_{yx}$ , and  $J_{yy}$  at the RGB wavelengths.

In the second stage, we replace the refractive lenses with metalenses in the  $4f$  system for CMOS-compatibility and massive production [19, 41–44]. It should be noted that in the aforementioned metasurface design,  $J_{ij} = |J_{ij}| \cdot e^{i\phi_{ij}}$  ( $i, j \in \{x, y\}$ ) describes the linear transformation of the input  $j$ -polarized component into the output  $i$ -polarized component, where  $\phi_{ij}$  represents the imparted geometrical phase [45] for each polarization component combination. The geometrical parameters of the metalens are searched in the same dataset as the metasurface.

We first define the target phase from the phase profile of an ideal lens:

$$\phi_{\text{lens}}(x, y, \lambda) = -\frac{2\pi}{\lambda} \left( \sqrt{x^2 + y^2 + f^2} - f \right) \quad (2)$$

where  $f$  is the design focal length and  $(x, y)$  denotes the position on the lens aperture. As shown in Fig. 1c, the target phase profile is discretized into 256 levels over  $[-\pi, \pi]$ . For each phase level, a candidate meta-atom is selected from the simulated dataset so that the co-polarized phase response matches the target phase as closely as possible while maintaining high transmission and low polarization crosstalk. The metalens design objective therefore combines phase error, transmission penalty, and polarization crosstalk penalty into a weighted scalar loss. This procedure is performed to determine the initial metalens geometries in both monochromatic and RGB-achromatic imaging.

The resulting monochromatic metalens performance is shown in Fig. 4a. The fitted phase profile agrees well with the target phase, yielding  $R^2 = 0.998$  and a phase MSE of 0.005128. Fig. 4b shows the objective intensity incident on the  $4f$  system. The sensor image in the output plane preserves the essential information, which further verifies that two such metalenses can form a  $4f$  system and provide a suitable initialization for the end-to-end optimization in the second stage.

## 2.2. Differentiable Optical Frontend

In the first stage, we consider a polarization-resolved  $4f$  system composed of two identical refractive lenses and a trainable metasurface ( $512 \times 512$ , pitch =  $0.4 \mu\text{m}$ ) located at the Fourier

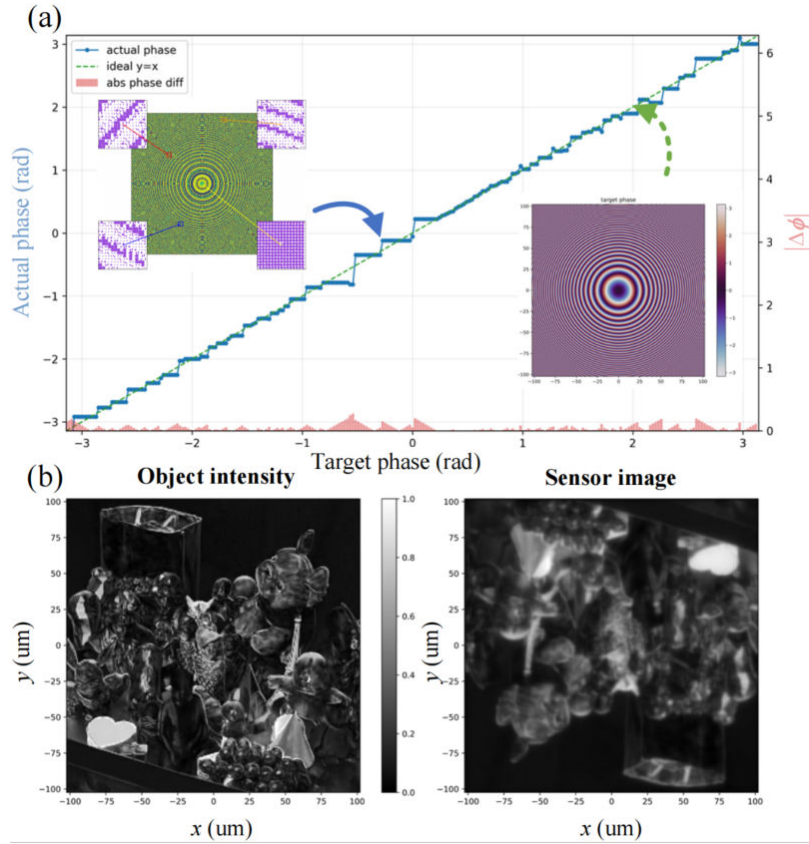


Fig. 4. The metalens performance in the monochromatic case at  $0.4358 \mu\text{m}$ . (a) The error and phase distribution of the actual phase and the target one. (b) The example of the real-world image propagates through meta-optic  $4f$  system.

plane, as shown in Fig. 2. The distances from the objective plane ( $256 \times 256$ , pitch =  $0.4 \mu\text{m}$ ) to the first lens  $z_1$  and from the second lens to the sensor plane  $z_2$  are both equal to the focal length  $f$  ( $0.5 \text{ mm}$ ). For each wavelength  $\lambda_k$ , the scene is represented by a spatially varying Jones field  $\mathbf{E}_{\text{in}}(\lambda_k)$ , derived from the target full-Stokes images. The field propagates through the first lens, the Fourier-plane metasurface, and the second lens before reaching the sensor ( $256 \times 256$ , pitch =  $0.4 \mu\text{m}$ ).

The entire forward pipeline can be formulated as below, and it holds true for all the RGB wavelengths:

$$\mathbf{E}_{\text{mask}} = \mathbf{J}_{\text{mask}} \mathbf{A}_{z_1} (\phi_{\text{lens}} \mathbf{A}_{z_1} (\mathbf{E}_{\text{in}})) \quad (3)$$

$$I_{\text{sensor}} = |\mathbf{A}_{z_2} (\phi_{\text{lens}} \mathbf{A}_{z_2} (\mathbf{E}_{\text{mask}}))|^2 \quad (4)$$

where  $\mathbf{J}_{\text{mask}}$  represents the Jones matrix of the metasurface,  $\phi_{\text{lens}}$  is the phase of two identical lenses.  $\mathbf{E}_{\text{mask}}$  is the output fields of the metasurface. To maintain differentiability for end-to-end optimization, we used the angular spectrum propagation method to model the free space propagation of light, where  $\mathbf{A}_{z_1}$  and  $\mathbf{A}_{z_2}$  represent the angular spectrum propagation operators corresponding to the distance  $z_1$  and  $z_2$ . The sensor measures only the scalar intensity  $I_{\text{sensor}}$ , which compresses the polarization and spectral information into a single channel.

In the second stage, the metalenses designed in Section 2.1, which are described by Jones

matrices  $J_{ml1}$  and  $J_{ml2}$ , are employed to replace the lenses for CMOS process compatibility and massive production. In the RGB case, a  $256 \times 256$  sensor measurement is used to reconstruct a  $256 \times 256 \times 4 \times 3$  full-Stokes data cube (pitch =  $0.4 \mu\text{m}$ ), corresponding to a compression ratio of 12. This makes the reconstruction strongly underdetermined and motivates joint optimization of both the optical frontend and the digital backend.

### 2.3. Backend

The polarization state of the incident field is represented by the full-Stokes parameters  $S_0$ ,  $S_1$ ,  $S_2$ , and  $S_3$ . Recovering these quantities ( $256 \times 256$ , pitch =  $0.4 \mu\text{m}$ ) from a single scalar sensor image constitutes a highly underdetermined problem, particularly in the RGB-achromatic case. To address this challenge, we employ a U-Net as the computational backend, as shown in Fig. 5. The architecture of U-Net utilizes a symmetric, hierarchical encoder-decoder structure with skip-connections to fuse multi-scale spatial features, which is crucial for maintaining the fidelity of complex polarization edges and textures that are often blurred in standard auto-encoders. The encoder path progressively processes the input through a series of double convolution blocks with  $3 \times 3$  convolutional layers, batch normalization, ReLU activation, and dropout with a rate of 0.1, reaching a bottleneck with 512 channels to extract compact abstract representations of the encoded Stokes information. Symmetrically, the decoder path reconstructs the spatial resolution via bilinear interpolation while incorporating the encoder's high-frequency details through skip-connections. A  $1 \times 1$  convolutional layer is employed at the output to project the decoded features to the target channel dimension, which can be dynamically adjusted based on the number of wavelengths. Additionally, a global residual learning strategy is adopted where the network predicts the deviation from a baseline constructed from the input intensity, facilitating faster convergence during optimization. For each wavelength, the network directly predicts the Stokes parameters.

Notably, U-Net exhibits strong translation invariance via its convolutional architecture, aligning well with the approximately linear shift-invariant (LSI) propagation model of the imaging system [46]. This makes it possible to naturally learn the spatial mapping from sensor intensity measurements to full-Stokes polarization parameters, efficiently overcoming the limitations of handcrafted priors in traditional regularization methods. Moreover, U-Net supports end-to-end optimization with relatively higher computational efficiency than iterative optimization-based

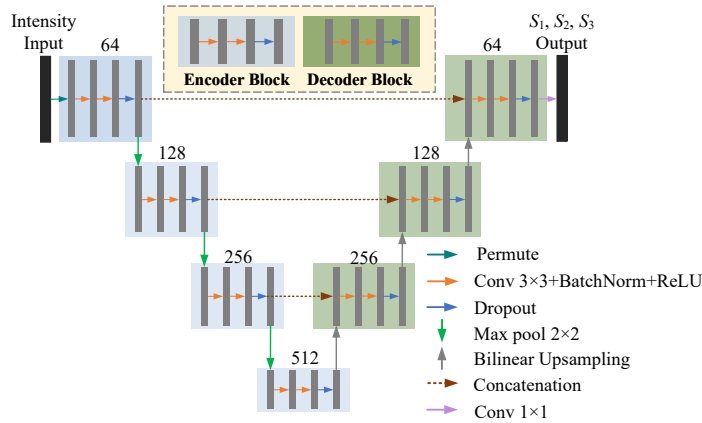


Fig. 5. Schematic overview of the U-Net used in the backend. The values above the block represent the number of feature maps produced at each stage.

methods.

#### 2.4. End-to-end collaboration

The system is optimized end-to-end based on a multi-objective loss function  $L_{\text{total}}$  that integrates the image reconstruction fidelity with hardware-level physical constraints to enhance physical consistency. The collaborative refinement ensures high PSNR and SSIM performance even at a significant compression ratio. The total loss  $L_{\text{total}}$  is defined as:

$$L_{\text{total}} = w_{\text{rec}}L_{\text{rec}} + w_{\text{ssim}}L_{\text{ssim}} + w_{\text{smooth}}L_{\text{smooth}} \quad (5)$$

where  $L_{\text{rec}}$  combines pixel-level  $L_1$  and  $L_2$  errors with a Sobel gradient loss to maintain high numerical accuracy and edge sharpness,  $L_{\text{ssim}}$  constrains the structural integrity of the reconstructed Stokes fields and  $L_{\text{smooth}}$  applies total variation (TV) regularization to the geometrical parameters to ensure spatial smoothness for fabrication and local periodic approximation. The loss weights  $w_{\text{rec}}$ ,  $w_{\text{ssim}}$ ,  $w_{\text{smooth}}$  are set to 10, 3, 0.01.

U-Net is trained jointly with the optical frontend using the Adam optimizer, a batch size of 4, and an early stop mechanism. The dataset is split into training/validation/test sets with a ratio of 8.5:1:0.5. The checkpoint with the lowest validation loss is selected for testing.

In the first stage (the blue arrows in Fig. 2), the trainable variables are the metasurface geometry, the focal length, and the neural-network weights. In the second stage (the purple arrows in Fig. 2), the trainable variables are the metasurface geometry, the two metalens geometries, the free-space distances, and the neural-network weights.

Gradients from  $L_{\text{total}}$  back propagate through the entire differentiable pipeline, following a chain rule framework for all tunable variables. The core gradient flow for the metasurface geometric parameters is  $\{a, b, \theta\}$  expressed as:

$$\frac{\partial L_{\text{total}}}{\partial \{a, b, \theta\}} = \frac{\partial L_{\text{total}}}{\partial U_{\varphi}} \cdot \frac{\partial U_{\varphi}}{\partial I_{\text{sensor}}} \cdot \frac{\partial I_{\text{sensor}}}{\partial E_{\text{mask}}} \cdot \frac{\partial E_{\text{mask}}}{\partial J_{\text{mask}}} \cdot \frac{\partial J_{\text{mask}}}{\partial \{a, b, \theta\}} \quad (6)$$

where  $U_{\varphi}$  represents the U-Net decoder function.

This formulation allows the optical encoder and the neural decoder to be refined jointly toward the same objective. Rather than optimizing the optics for a predefined polarization response and training the network afterward, the proposed framework learns an optical encoding strategy that directly matches the reconstruction task and the statistics of the dataset.

### 3. Results and discussion

We evaluate the proposed framework on the real-world spectro-polarimetric dataset [30], which contains 2022 samples and exhibits substantially richer spatial, spectral, and polarization statistics than the synthetic datasets commonly used in prior works. The dataset is divided into the training, validation and test sets. The optical setups in two stages are considered across Section 3.1 and 3.2: a hybrid metasurface-refractive  $4f$  system in the first stage and a pure meta-optic  $4f$  system in the second stage where the refractive lenses are replaced by metalenses. For each setup, to rigorously evaluate the reconstruction capability of the proposed framework, we study both monochromatic and RGB reconstruction and compare three metasurface mask settings: a jointly optimized trained mask initialized with random geometric parameters, a fixed random mask with random geometric parameters, and a no-mask baseline without the metasurface, where only the U-Net in the backend is optimized for the latter two cases. The framework is trained on an NVIDIA GeForce RTX 5090.

#### 3.1. Real-world dataset testing with lenses in the first stage

In the first stage, where a  $4f$  system with conventional refractive lenses is employed, metasurface is initialized to a random structure as a trained mask and then jointly optimized with the focal

length  $f$  and neural-network weights  $\varphi$ .

### 3.1.1. Monochromatic reconstruction

The training is based on the early stop mechanism. The corresponding training curves for the monochromatic case are shown in Fig. 6. The trained-mask configuration achieves a substantially lower validation loss ( $\approx 0.4$ ) by epoch 183 within 2.95 hrs, compared with the random-mask and no-mask baselines which yield validation losses around 1.0 at epochs 165 and 208. This demonstrates that joint optical-digital optimization improves the conditioning of the inverse problem. In other words, the optimized metasurface produces sensor measurements that are more informative for downstream Stokes recovery than either a random encoding or no encoding at all.

The optimized phase profile of the trained-mask metasurface is shown in Fig. 7(a), exhibiting no obvious regular pattern. This is a natural outcome of the optimization process, demonstrating the ability of the optimization to discover non-intuitive distributions that are difficult for humans to come up with.

The quantitative comparison results under different masks are summarized in Table 2. The

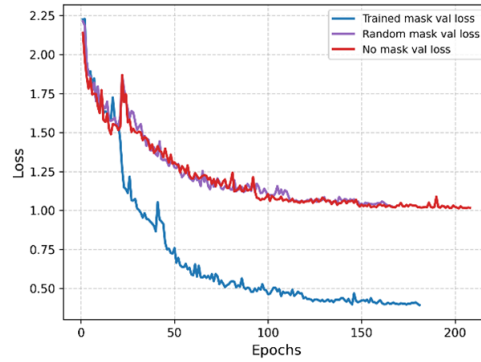


Fig. 6. Loss function under different masks over training epochs in the monochromatic case for the first stage.

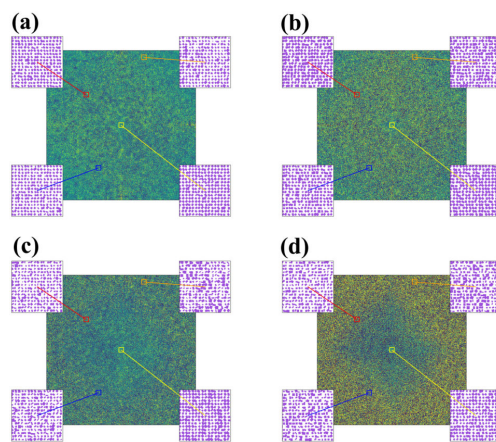


Fig. 7. The phase profiles of the trained-mask metasurface after end-to-end training: (a) monochromatic case for the first stage (b) RGB-achromatic case for the first stage (c) monochromatic case for the second stage (d) RGB-achromatic case for the second stage.

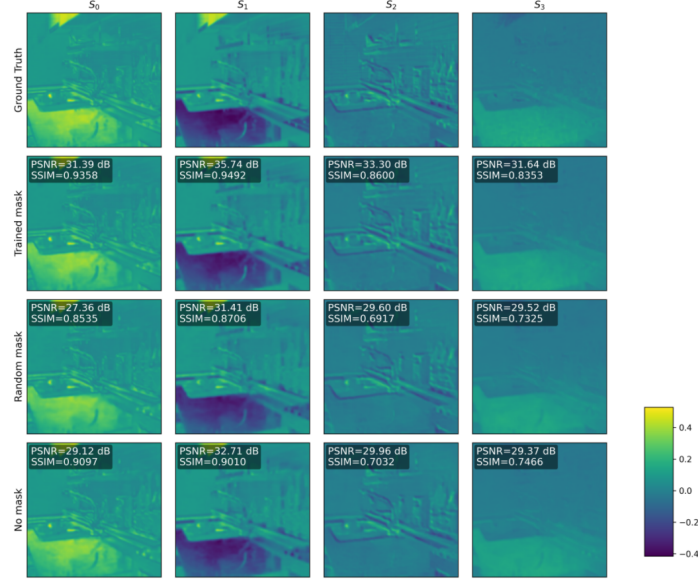


Fig. 8. Examples of full-Stokes images reconstructed under different masks in the monochromatic case for the first stage.

Table 2. Quantitative comparison of PSNR, SSIM, MSE and FPS under different masks in the monochromatic case for the first stage.

Methods	Trained mask	Random mask	no mask
PSNR (dB)	30.00	24.85	25.45
SSIM	0.8291	0.6159	0.6455
MSE	$4.34 \times 10^{-4}$	$1.40 \times 10^{-3}$	$1.34 \times 10^{-3}$
FPS (imgs/s)	151.58	152.06	151.85

trained-mask configuration achieves an average PSNR of 30.00 dB and an average SSIM of 0.8291, compared with 24.85 dB and 0.6159 for the random-mask baseline and 25.45 dB and 0.6455 for the no-mask baseline. This corresponds to a PSNR gain of 5.15 dB over the random-mask case and 4.55 dB over the no-mask case, together with substantial SSIM improvements. The MSE is reduced from  $1.40 \times 10^{-3}$  and  $1.34 \times 10^{-3}$  in the two baselines to  $4.34 \times 10^{-4}$  in the trained-mask setting, representing roughly a threefold error reduction. Given the fast transmission speed of physical front-end, we only evaluate the inference speed in the backend. The inference speed remains essentially unchanged at approximately 152 imgs/s, which indicates that the performance gain arises from improved optical encoding rather than additional computational cost in the decoder.

Representative reconstructions are shown in Fig. 8. The trained-mask configuration more accurately preserves fine structures and spatial boundaries in the reconstructed Stokes images, whereas the random-mask and no-mask baselines exhibit blurrier edges and a greater loss of local polarization detail. These results confirm that, even in the monochromatic setting, end-to-end optimization yields a measurable advantage over both fixed random encoding and

purely computational reconstruction.

### 3.1.2. RGB-achromatic reconstruction

The RGB reconstruction task is significantly more challenging because the sensor must encode the full-Stokes parameters at three wavelengths into a single intensity image with a high compression ratio of 12. Despite this stronger compression, the trained-mask system achieves stable convergence by epoch 175, whereas the random-mask and no-mask baselines stop at epochs 192 and 170 as shown in Fig. 9. The trained mask learns a wavelength- and polarization-dependent measurement operator that allows the U-Net to disentangle the multiplexed information more effectively than in the random-mask and no-mask baselines. The training time of the trained mask is 7.99 hrs. The optimized phase profile of the trained-mask metasurface is shown in Fig. 7(b).

Table 3 summarizes the quantitative comparisons for the RGB-achromatic cases. The trained-mask configuration achieves an average PSNR of 26.71 dB and an average SSIM of 0.7044, compared with 23.11 dB and 0.5478 for the random-mask baseline and 23.60 dB and 0.5803 for the no-mask baseline. Relative to the random-mask case, the jointly optimized system improves PSNR by 3.60 dB and SSIM by 0.1566. Relative to the no-mask baseline, the gains are 3.11 dB and 0.1241, respectively. Compared to the monochromatic value, although the MSE increases to  $8.24 \times 10^{-4}$ , it remains lower than those of the baselines, which are on the order of  $10^{-3}$ . The inference speed remains high, with the trained-mask configuration reaching 148.54 imgs/s.

The visual results in Fig. 10 show that the proposed system maintains good reconstruction fidelity across different wavelength channels and Stokes components despite the high compression ratio of 12. Compared with the baselines, the trained-mask system better preserves both spectral consistency and polarization-dependent contrast. This result is important because it shows that the benefit of end-to-end optical design is not limited to the monochromatic case but extends to high-dimensional RGB full-Stokes recovery.

### 3.2. Real-world dataset testing with metalenses in the second stage

In the second stage, the two refractive lenses are replaced by metalenses, yielding a pure meta-optic  $4f$  system for CMOS process compatibility and massive production. At this point, the trainable focal-length parameter is replaced by the free-space distances  $z_1$  and  $z_2$ . The same three mask settings are used for comparison.

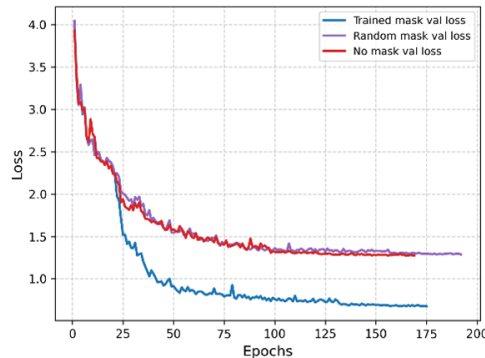


Fig. 9. Loss function under different masks over training epochs in the RGB-achromatic case for the first stage.

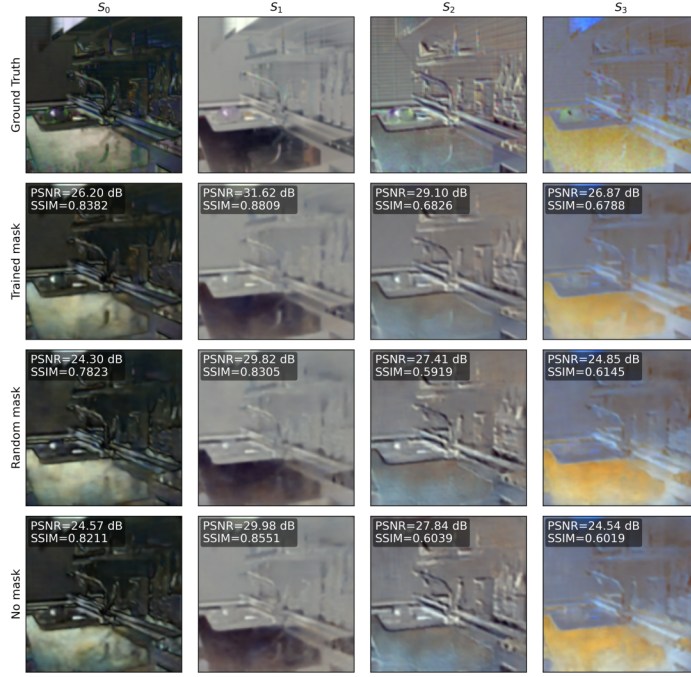


Fig. 10. Examples of full-Stokes images reconstructed under different masks in the RGB-achromatic case for the first stage.

Table 3. Quantitative comparison of PSNR, SSIM, MSE and FPS under different masks in the RGB-achromatic case for the first stage.

Methods	Trained mask	Random mask	no mask
PSNR (dB)	26.71	23.11	23.60
SSIM	0.7044	0.5478	0.5803
MSE	$8.24 \times 10^{-4}$	$2.03 \times 10^{-3}$	$1.83 \times 10^{-3}$
FPS (imgs/s)	148.54	142.15	143.77

### 3.2.1. Monochromatic reconstruction

The monochromatic training dynamics are shown in Fig. 11. The trained-mask configuration again converges to a lower validation loss ( $\approx 0.5$ ) by epoch 195 within the training time of 11.08 hrs than the random-mask ( $\approx 1.9$ ) and no-mask ( $\approx 1.7$ ) baselines by epochs 33 and 110, although the final loss is higher than that of the metasurface-refractive first stage. This behavior is consistent with the increased difficulty of the pure meta-optic system, where residual phase mismatch, aperture discretization, and optical nonidealities make the forward operator harder to invert. The optimized phase profile of the trained-mask metasurface is shown in Fig. 7(c).

The quantitative performance is listed in Table 4. The trained-mask configuration achieves an average PSNR of 26.94 dB and an average SSIM of 0.7184, compared with 18.74 dB and 0.3309 for the random-mask baseline and 20.51 dB and 0.4346 for the no-mask baseline. Thus, even in the pure meta-optic system, end-to-end optimization improves PSNR by 8.20 dB over

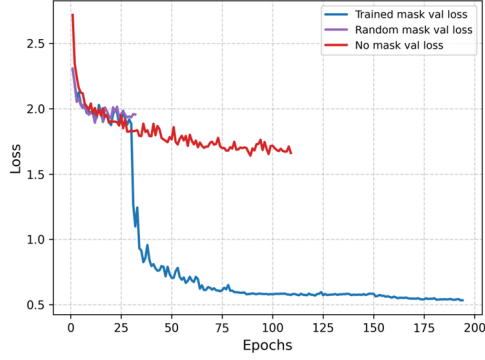


Fig. 11. Loss function under different masks over training epochs in the monochromatic case for the second stage.

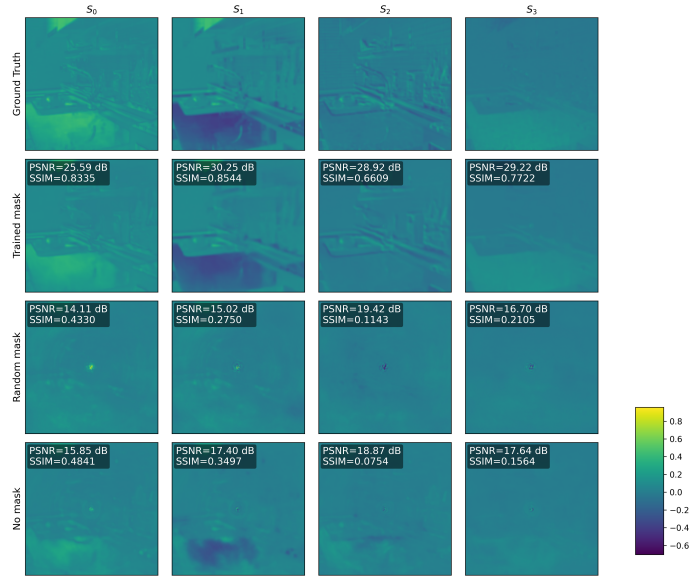


Fig. 12. Examples of full-Stokes images reconstructed under different masks in the monochromatic case for the second stage.

the random-mask case and by 6.43 dB over the no-mask case. The corresponding MSE of the trained-mask system is  $7.58 \times 10^{-4}$ , which is smaller than those of the baselines. The inference speed remains high, between 144 and 151 imgs/s.

Visual results in Fig. 12 demonstrate that the trained mask preserves image textures and Stokes parameters contrast, whereas the random-mask and no-mask cases display strong concentric artifacts. These artifacts are primarily caused by phase discretization and the resulting parasitic diffraction of the metalenses. Without an optimized phase profile, these discrete phase errors manifest as the geometric signature of the circular aperture, leading to an encoding collapse. The reconstruction backend fails to distinguish true object features from this systematic diffraction noise.

Table 4. Quantitative comparison of PSNR, SSIM, MSE and FPS under different masks in the monochromatic case for the second stage.

Methods	Trained mask	Random mask	no mask
PSNR (dB)	26.94	18.74	20.51
SSIM	0.7184	0.3309	0.4346
MSE	$7.58 \times 10^{-4}$	$5.03 \times 10^{-3}$	$3.21 \times 10^{-3}$
FPS (imgs/s)	150.58	146.09	144.70

### 3.2.2. RGB-achromatic reconstruction

The RGB-achromatic training results are shown in Fig. 13. Although in the monochromatic case, the trained-mask configuration achieves a substantially lower validation loss than the baselines, the gap between the trained-mask and baseline curves is even larger here because the RGB task is more severely underdetermined. The validation loss for the trained-mask configuration drops sharply around epoch 35 and keeps decreasing steadily to approximately 0.9. The trained-mask configuration trains until epoch 152, considerably later than the random-mask and no-mask baselines, which early stop at epochs 56 and 54, owing to the benefits of joint meta-optic optimization, especially for such a challenging inverse problem. The training time within the trained mask is 11.69 hrs. The optimized phase profile of the trained-mask metasurface is shown in Fig. 7(d).

The trained-mask meta-optic system reaches an average PSNR of 24.10 dB and an average SSIM of 0.6015 at the RGB wavelengths (Table 5), compared with 18.83 dB and 0.3335 for the random-mask baseline and 19.26 dB and 0.3521 for the no-mask baseline. This corresponds to PSNR gains of 5.27 dB and 4.84 dB, respectively, together with marked SSIM improvements. The MSE of the trained-mask system is  $1.55 \times 10^{-3}$ , still significantly smaller than those of the baselines. The inference speed remains close to 150 imgs/s, demonstrating that the pure meta-optic configuration does not compromise the real-time capability of the neural decoder.

As shown in Fig. 14, the trained-mask system reconstructs RGB full-Stokes information with clearly better spatial detail and fewer artifacts than the baselines. The random-mask and no-mask systems exhibit even stronger concentric artifacts regarding chromatic dispersion and phase

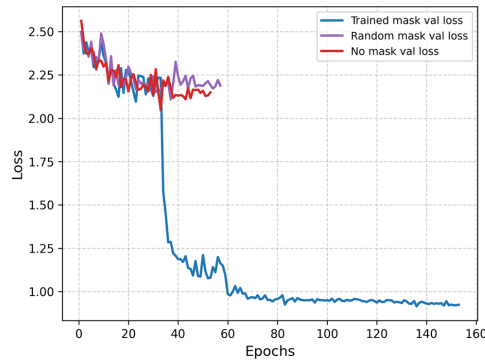


Fig. 13. Loss function under different masks over training epochs in the RGB-achromatic case for the second stage.

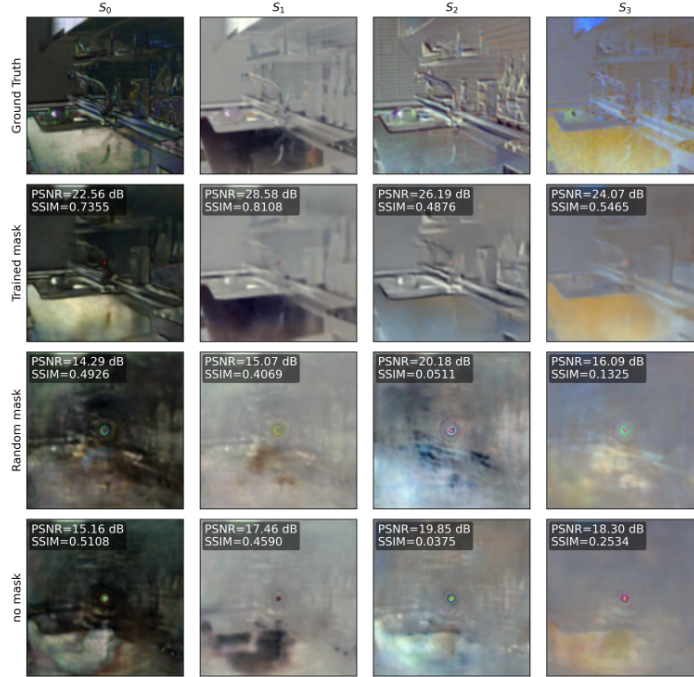


Fig. 14. Examples of full-Stokes images reconstructed under different masks in the RGB-achromatic case for the second stage.

Table 5. Quantitative comparison of PSNR, SSIM, MSE and FPS under different masks in the RGB-achromatic case for the second stage.

Methods	Trained mask	Random mask	no mask
PSNR (dB)	24.10	18.83	19.26
SSIM	0.6015	0.3335	0.3521
MSE	$1.55 \times 10^{-3}$	$5.47 \times 10^{-3}$	$4.67 \times 10^{-3}$
FPS (imgs/s)	149.50	148.81	143.19

discretization. Although the RGB meta-optic performance is lower than that of the refractive lenses in the first stage, the results demonstrate that a pure meta-optic architecture can still support high-dimensional full-Stokes reconstruction by jointly optimizing the optical encoder and the digital decoder.

### 3.3. Full-Stokes reconstruction performance comparison

To place the results in context, Table 6 compares the proposed framework with representative full-Stokes reconstruction systems reported in the literature. Direct numerical comparison should be interpreted with caution because the reported methods differ in wavelength range, compression setting, dataset type, meta-optic architecture, and evaluation protocol. In particular, many prior works are evaluated on synthetic datasets [4, 25, 47], whereas our results are obtained on a real-world spectro-polarimetric dataset with more complex scenes in which the light from the

scenes has real-world polarization information.

Within this context, the proposed framework remains competitive while operating under aggressive compression. In the hybrid refractive-metasurface system, the monochromatic configuration achieves 30.00 dB PSNR and 0.8291 SSIM at a compression ratio of 4, while the RGB configuration achieves 26.71 dB and 0.7044 at a compression ratio of 12. In the pure meta-optic  $4f$  system, the corresponding values are 26.94 dB and 0.7184 for the monochromatic case and 24.10 dB and 0.6015 for the RGB case. These results show that the proposed end-to-end inverse designed framework can maintain high reconstruction fidelity even when both spectral and polarization information are significantly compressed into a single measurement.

More importantly, the comparison across Tables 2–5 shows that the main advantage of the framework does not arise merely from using a neural decoder, but from jointly optimizing the optical encoder and the reconstruction network. Across both stages and both wavelength settings, the trained-mask configuration consistently outperforms the random-mask and no-mask baselines. This trend demonstrates that in snapshot full-Stokes imaging, the quality of the encoded measurement is as critical as the power of the reconstruction algorithm.

Table 6. Parameters and Performance of the State-of-the-Arts Snapshot Full-Stokes Reconstruction Works.

Wavelength (nm)	Compression ratio	Dataset	Meta-optic architecture	MSE	PSNR	SSIM	Ref.
808	0.064	Synthetic	Pure	/	41.71	/	[4]
530	4	Synthetic	Hybrid	/	28.09	0.8465	[47]
532	4	Synthetic	Hybrid	$3.61 \times 10^{-4}$	39.46	0.9430	[25]
435.8	4	<b>Real-world</b>	Hybrid	$4.34 \times 10^{-4}$	30.00	0.8291	Ours (lens)
435.8, 546.1, 700	<b>12</b>	<b>Real-world</b>	Hybrid	$8.24 \times 10^{-4}$	26.71	0.7044	Ours (lens)
435.8	4	<b>Real-world</b>	Pure	$7.58 \times 10^{-4}$	26.94	0.7184	Ours (metalens)
435.8, 546.1, 700	<b>12</b>	<b>Real-world</b>	Pure	$1.55 \times 10^{-3}$	24.10	0.6015	Ours (metalens)

\* **Pure**: The system only contains meta-optics.

\* **Hybrid**: The system contains meta-optics and conventional optical elements (e.g., lenses, polarizers).

\* **Real-world dataset**: Captured from naturally occurring scenes with genuine, uncontrolled physical interactions and real-world polarization information, not imposed by designed labels.

\* **Synthetic dataset**: Any dataset outside this definition, including simulated, generated, staged, or artificially controlled measurements.

#### 4. Summary and outlook

In summary, we have presented an end-to-end framework for snapshot full-Stokes polarization imaging that jointly optimizes a meta-optic frontend and a neural reconstruction backend. By employing a trainable metasurface surrogate model, the differentiable frontend learns an optical measurement operator tailored for full-Stokes polarization recovery rather than intensity-only target. This strategy is effective in a hybrid metasurface-refractive system and a pure meta-optic system. Notably, on a real-world dataset, the framework reconstructs monochromatic and RGB-achromatic full-Stokes images from a snapshot measurement, with the RGB configuration operating at a high compression ratio of 12.

Beyond the absolute reconstruction metrics, the central result is that co-designed optical encoding substantially improves the reconstructability of the inverse problem relative to fixed or

unstructured encoders. The main reason for the performance gain does not arise merely from a stronger reconstruction network, but from learning a task-specific optical encoder jointly with the digital decoder. This is especially important for full-Stokes imaging, where spectral and polarization information must be compressed into a single information channel under realistic physical constraints. This result supports the central premise of end-to-end meta-optical imaging: for highly compressed inverse problems, the quality of the encoded measurement is as important as the expressive power of the reconstruction algorithm. The example metasurfaces and metalenses designed in this work are experimentally feasible, composed of rectangular nanopillars.

Looking forward, the remaining gap between the hybrid and pure meta-optic configurations shows that for each optical element compactness still trades against optical quality when refractive optics are replaced by meta-optics. Future work should therefore focus on more compact, fabrication-robust and sensor-aware system designs that are compatible with practical pixel sizes and more expressive optical devices such as multi-layer or nonlocal metasurfaces [48–50]. Extending the present framework from three isolated wavelengths to continuous spectral bands and from static scenes to dynamic polarimetric imaging could further promote compact machine vision, remote sensing, and physical informed imaging [51, 52]. Within that broader trajectory, the present work shows that meta-optics can be used not only as ultrathin replacements for conventional optical elements, but as learned physical encoders whose function is defined directly by the downstream inference task. We therefore expect end-to-end optical–digital co-design to become an increasingly important route toward compact, application-ready polarization imaging systems.

**Funding.** Advanced Materials – National Science and Technology Major Project (2025ZD0616302); the National Natural Science Foundation of China (62275046); the Jiangsu Province Frontier Research Project (BF2024061); Big Data Computing Center of Southeast University and the Center for Fundamental and Interdisciplinary Sciences of Southeast University.

**Disclosures.** The authors declare no conflicts of interest.

**Data Availability Statement.** Data underlying the results presented in this paper are not publicly available at this time but may be obtained from the authors upon reasonable request.

**Supplemental document.** No supplementary materials are available.

## References

1. G. E. Walter, “Polarization and surface roughness,” in *PROCEEDINGS OF SPIE*, vol. 3426 (1998), pp. 144–152.
2. S.-Y. Lu and R. A. Chipman, “Interpretation of mueller matrices based on polar decomposition,” *J. Opt. Soc. Am. A* **13**, 1106–1113 (1996).
3. B. C. David and J. L. Pezzaniti, “Polarization imaging through scattering media,” in *PROCEEDINGS OF SPIE*, vol. 4133 (2000), pp. 124–133.
4. X. Ren, Y. Tian, Y. Ren, *et al.*, “Single-shot full-stokes imaging through scattering media,” *Optica* **12**, 1560–1568 (2025).
5. Z. Xie, W. Lin, M. Zhu, *et al.*, “Reciprocal polarization imaging of complex media,” *Adv. Photonics Nexus* **4**, 036010 (2025).
6. J. Wang, C. Jiang, W. Li, and X. Xiao, “Anisotropic low-dimensional materials for polarization-sensitive photodetectors: From materials to devices,” *Adv. Opt. Mater.* **10**, 2102436 (2022).
7. S. Song, J. Kim, T. Moon, *et al.*, “Polarization-sensitive intensity diffraction tomography,” *Light. Sci. & Appl.* **12**, 124 (2023).
8. S. Zhou, J. Bian, P. Chen, *et al.*, “Polarization-dispersive imaging spectrometer for scattering circular dichroism spectroscopy of single chiral nanostructures,” *Light. Sci. & Appl.* **11**, 64 (2022).
9. F. Neubrech, M. Hentschel, and N. Liu, “Reconfigurable plasmonic chirality: Fundamentals and applications,” *Adv. Mater.* **32**, 1905640 (2020).
10. S. Chen, P. Liu, W. He, *et al.*, “Polarization-enhanced underwater laser range-gated imaging for subaquatic applications,” *Sensors* **24**, 6681 (2024).
11. L. B. Wolff, “Polarization vision: a new sensory approach to image understanding,” *Image Vis. Comput.* **15**, 81–93 (1997).
12. Y. Lei, B. Lei, Y. Cai, *et al.*, “Polarimetric dehazing method based on image fusion and adaptive adjustment algorithm,” *Appl. Sci.* **11**, 10040 (2021).

13. Z. Liu, Z. Song, Z. Li, and L. Li, "Integrated polarimetric spectral imaging sensor combining spectral imaging and polarization modulation techniques," *Sensors* **26**, 144 (2025).
14. A. Peinado, A. Lizana, and J. Campos, "Optimization and tolerance analysis of a polarimeter with ferroelectric liquid crystals," *Appl. Opt.* **52**, 5748–5757 (2013).
15. V. Gruev, R. Perkins, and T. York, "Ccd polarization imaging sensor with aluminum nanowire optical filters," *Opt. Express* **18**, 19087–19094 (2010).
16. J. Ma, Z. Yu, Z. Li, *et al.*, "Integrated diffractive full-stokes spectro-polarimetric imaging," *Opt. Express* **33**, 51223–51236 (2025).
17. D. Pierangeli, G. Volpe, and C. Conti, "Deep learning enabled transmission of full-stokes polarization images through complex media," *Laser & Photonics Rev.* **18**, 2400626 (2024).
18. D. Pierangeli and C. Conti, "Single-shot polarimetry of vector beams by supervised learning," *Nat. Commun.* **14**, 1831 (2023).
19. M. Khorasaninejad, W. T. Chen, R. C. Devlin, *et al.*, "Metalenses at visible wavelengths: Diffraction-limited focusing and subwavelength resolution imaging," *Science* **352**, 1190–1194 (2016).
20. W. T. Chen, J.-S. Park, J. Marchioni, *et al.*, "Broadband, high-efficiency metasurfaces using dispersion-engineered nanostructures," in *Conference on Lasers and Electro-Optics (CLEO) 2024*, (Optica Publishing Group, 2024), p. FM3L.7.
21. Z. Jun-zhuo, H. A. O. Jia, Y. U. Xiao-chang, *et al.*, "Recent advances in metasurfaces for polarization imaging," *Chin. Opt.* **16**, 973–995 (2023).
22. J. P. Balthasar Mueller, N. A. Rubin, R. C. Devlin, *et al.*, "Metasurface polarization optics: Independent phase control of arbitrary orthogonal states of polarization," *Phys. Rev. Lett.* **118**, 113901 (2017).
23. P. Thrane, C. Meng, A. Bykov, *et al.*, "Reflective metagrating polarimeter for single-shot full-stokes mapping: toward digital histopathology," *Light. Adv. Manuf.* **7**, 1 (2026).
24. S.-H. Baek, H. Ikoma, D. S. Jeon, *et al.*, "Single-shot hyperspectral-depth imaging with learned diffractive optics," in *Proceedings of the IEEE/CVF International Conference on Computer Vision*, (2021), pp. 2651–2660.
25. H. Xia, B. Chen, C. Zhang, *et al.*, "Joint optimization of coded aperture metasurface and residual self-attention network for snapshot full-stokes imaging," *Opt. Express* **32**, 29609–29619 (2024).
26. G. Arya, W. F. Li, C. Roques-Carmes, *et al.*, "End-to-end optimization of metasurfaces for imaging with compressed sensing," *ACS Photonics* **11**, 2077–2087 (2024).
27. Z. Lin, R. Pestourie, C. Roques-Carmes, *et al.*, "End-to-end metasurface inverse design for single-shot multi-channel imaging," *Opt. Express* **30**, 28358–28370 (2022).
28. Z. Lin, C. Roques-Carmes, R. Pestourie, *et al.*, "End-to-end nanophotonic inverse design for imaging and polarimetry," *Nanophotonics* **10**, 1177–1187 (2021).
29. S. Fisher, G. Arya, A. Majumdar, *et al.*, "End-to-end metasurface design for temperature imaging via broadband planck-radiation regression," *Adv. Opt. Mater.* **13**, 2402498 (2025).
30. Y. Jeon, E. Choi, Y. Kim, *et al.*, "Spectral and polarization vision: Spectro-polarimetric real-world dataset," in *2024 IEEE/CVF Conference on Computer Vision and Pattern Recognition (CVPR)*, (2024), pp. 22098–22108.
31. Z. Li, R. Pestourie, J.-S. Park, *et al.*, "Inverse design enables large-scale high-performance meta-optics reshaping virtual reality," *Nat. Commun.* **13**, 2409 (2022).
32. R. Pestourie, W. Yao, B. Kanté, and S. G. Johnson, "Efficient inverse design of large-area metasurfaces for incoherent light," *ACS Photonics* **10**, 854–860 (2023).
33. L. Sacchi, A. Palmieri, V. Mishra, *et al.*, "Silica meta-optics: When high performance does not need a high index," *Nano Lett.* **25**, 17448–17457 (2025).
34. N. A. Rubin, A. Zaidi, A. H. Dorrah, *et al.*, "Jones matrix holography with metasurfaces," *Sci. Adv.* **7**, eabg7488 (2021).
35. A. F. Oskooi, D. Roundy, M. Ibanescu, *et al.*, "Meep: A flexible free-software package for electromagnetic simulations by the fdtd method," *Comput. Phys. Commun.* **181**, 687–702 (2010).
36. R. Pestourie, C. Pérez-Arancibia, Z. Lin, *et al.*, "Inverse design of large-area metasurfaces," *Opt. Express* **26**, 33732–33747 (2018).
37. Z. Lin, V. Liu, R. Pestourie, and S. G. Johnson, "Topology optimization of freeform large-area metasurfaces," *Opt. Express* **27**, 15765–15775 (2019).
38. R. Pestourie, C. Pérez-Arancibia, Z. Lin, *et al.*, "Inverse design of large-area metasurfaces," *Opt. Express* **26**, 33732–33747 (2018).
39. H. Chung, F. Zhang, H. Li, *et al.*, "Inverse design of high-na metalens for maskless lithography," *Nanophotonics* **12**, 2371–2381 (2023).
40. E. Bayati, R. Pestourie, S. Colburn, *et al.*, "Inverse designed metalenses with extended depth of focus," *ACS Photonics* **7**, 873–878 (2020).
41. W. T. Chen, A. Y. Zhu, V. Sanjeev, *et al.*, "A broadband achromatic metalens for focusing and imaging in the visible," *Nat. Nanotechnol.* **13**, 220–226 (2018).
42. Z. Li, P. Lin, Y.-W. Huang, *et al.*, "Meta-optics achieves rgb-achromatic focusing for virtual reality," *Sci. Adv.* **7**, eabe4458 (2021).
43. M. Khorasaninejad, A. Y. Zhu, C. Roques-Carmes, *et al.*, "Polarization-insensitive metalenses at visible wavelengths," *Nano Lett.* **16**, 7229–7234 (2016).

44. M. Sun, A. Shakeri, A. Keshvari, *et al.*, “Scalable freeform optimization of wide-aperture 3d metalenses by zoned discrete axisymmetry,” *ACS Photonics* **12**, 3163–3171 (2025).
45. A. Arbabi, Y. Horie, M. Bagheri, and A. Faraon, “Dielectric metasurfaces for complete control of phase and polarization with subwavelength spatial resolution and high transmission,” *Nat. Nanotechnol.* **10**, 937–943 (2015).
46. W. F. Li, G. Arya, C. Roques-Carmes, *et al.*, “Transcending shift-invariance in the paraxial regime via end-to-end inverse design of freeform nanophotonics,” *Opt. Express* **31**, 24260–24272 (2023).
47. H. Xia, Q. Zhang, C. Zhang, *et al.*, “Inverse design of cascaded multidimensional coding metasurface for snapshot full-stokes imaging and depth estimation,” *ACS Photonics* **12**, 6502–6510 (2025).
48. L. Stefanini, D. Ramaccia, M. Barbuto, *et al.*, “A statistical approach for robust metasurfaces and metasurface-based ris engineering,” *IEEE Trans. on Antennas Propag.* **72**, 5402–5407 (2024).
49. Y. Zhou, I. I. Kravchenko, H. Wang, *et al.*, “Multilayer noninteracting dielectric metasurfaces for multiwavelength metaoptics,” *Nano letters* **18**, 7529–7537 (2018).
50. G. Yang, M. Wang, J. S. Lee, *et al.*, “Nonlocal phase-change metaoptics for reconfigurable nonvolatile image processing,” *Light. Sci. & Appl.* **14**, 182 (2025).
51. S. Colburn, A. Zhan, and A. Majumdar, “Metasurface optics for full-color computational imaging,” *Sci. Adv.* **4**, eaar2114 (2018).
52. L. Huang, Z. Han, A. Wirth-Singh, *et al.*, “Broadband thermal imaging using meta-optics,” *Nat. Commun.* **15**, 1662 (2024).